Wind Energy

WILEY

RESEARCH ARTICLE OPEN ACCESS

Support Structure Modelling in Actuator Line Method Large Eddy Simulations of Wind Turbine Wakes

Markella Zormpa | Christopher R. Vogel | Richard H. J. Willden

Department of Engineering Science, University of Oxford, Oxford, UK

Correspondence: Markella Zormpa (markella.zormpa@eng.ox.ac.uk)

Received: 27 December 2024 | **Revised:** 23 October 2025 | **Accepted:** 3 November 2025

Keywords: actuator line method | large eddy simulation | nacelle | support structure | tower | wind turbine wakes

ABSTRACT

While advancements in the prediction of wind turbine loads and wakes within the actuator line method large eddy simulation (ALM-LES) framework have been an active research topic in recent years, the modelling of the tower and nacelle has received comparatively less attention. This paper investigates different numerical modelling methods for the representation of the support structure and discusses the implications and trade-offs associated with each method. Three support structure modelling approaches are investigated: explicitly meshing the support structure, a direct forcing meshless representation and a combination of actuator disc/line method for the representation of the nacelle/tower. All methods contribute to a more realistic representation of the near wake mean flow when compared with experimental measurements. In the measured far wake, the interaction between the tower and rotor wakes creates asymmetries in the mean flow profiles. The meshed and cell-blocking numerical representations are capable of replicating these far wake asymmetries, whereas the actuator line/disc method does not capture these features.

1 | Introduction

Given the significant impact that wind turbine wakes have on wind farm efficiency, it is imperative to be able to predict these flows accurately. Inaccurate engineering wake models can have various consequences, including loss of revenue for wind plant developers, and the large uncertainty may result in marginal projects not being developed; see Veers et al. [1] for a thorough review. Inaccurate wake modelling also creates a bottleneck in efforts to exploit wake aerodynamics in wind farm design and control.

Wind turbine wakes are complex multiscaled aerodynamic phenomena characterised as simultaneously high Reynolds and low Mach number flows. The large range of spatial and temporal scales of turbine wakes are difficult to resolve in well-characterised conditions at utility scale, and it is challenging to capture the relevant physics in scaled wind turbine tests given the differences in flow regimes that can be reproduced. It is often the case that high-fidelity numerical simulations can provide the richest dataset for the study of wake flows. When simulating wind turbine wakes, the turbine nacelle and tower—collectively the support structure—has often been omitted from the simulations for simplicity. However, there has been consistent evidence that suggests that towers and nacelles can affect wind flows at various spatial scales and in non-trivial ways. A brief review of the current understanding of the effect of support structures in wind energy problems is presented below across four different scales: the blade, the near wake, far wake and wind farm aerodynamics.

The support structure impacts the *blade aerodynamics* of the turbine and therefore the overall power and thrust of the rotor. The tower creates a tower shadow effect: The tower structure

This is an open access article under the terms of the Creative Commons Attribution License, which permits use, distribution and reproduction in any medium, provided the original work is properly cited.

© 2025 The Author(s). *Wind Energy* published by John Wiley & Sons Ltd.

decelerates the local incident velocity, and as a result, when the blade is passing upstream of the tower, local blade forces are typically reduced due to both a reduction in available kinetic energy and a perturbation to the local flow angle. The blade of an upwind turbine experiences an instantaneous drop of normal and tangential force that may be of the order of 5% [2, 3], depending on many factors such as the tower diameter, operating conditions, overhang and others. When averaged across an entire rotation, the change in mean blade forces appears less pronounced, but the rotor fatigue loads are significant and routinely considered in wind turbine design [4].

The presence of the nacelle, on the other hand, may lead to a slight increase in the incident velocity on the inboard sections of the rotor when compared with simulations that ignore the presence of the nacelle and allow air to flow through the low-resistance centre of the rotor instead. This can lead to differences in the simulated wake dynamics.

The *near wake* of an upwind rotor directly interacts with the nacelle and tower wakes. Pierella and Sætran [5] experimentally studied near wake velocity fields up to three diameters downstream of the rotor. They identified the wake of the tower as a low velocity region that developed directly downstream of the tower and disrupted assumed axisymmetry of the rotor wake. Moving downstream, the tower wake was rotated by the rotor wake, intensifying the introduced asymmetry in the combined wake. This asymmetry eventually led to an azimuthal imbalance in momentum entrainment into the wake, causing a vertical drop of the centre of the wake. In this work, the dataset by Pierella and Sætran is extended by simulating the far wake of the above case.

Coherent structures shed from the tower and nacelle interact with the wind turbine wake structures changing the overall near wake vorticity map as demonstrated by Debnath et al. [6]. Proper orthogonal decomposition analysis of a wind turbine wake excluding and including the support structure showed that the principal tip vortex breakdown mechanism was altered due to the presence of the tower. Additionally, the presence of the nacelle was found to eliminate the root vortices, also observed experimentally by Sherry et al. [7].

The effect of the nacelle alone has been studied in the literature and linked to near and far wake features. The mean centreline velocity downstream of the nacelle has been reported in measurements and simulations as either a local minimum [8, 9] or a local maximum [10]. Abraham et al. [10] noted that in studies that employ utility-scale rotors, a local maximum can be expected: Utility-scale rotors are characterised by a small nacelle to rotor diameter ratio, $D_{nac}/D \approx 5\%$, and the inboard sections of their blades consist of cylindrical sections with low axial induction that may be responsible for the observed acceleration at hub height. On the other hand, small experimental rotors are characterised by $D_{nac}/D \approx 10\%$ and blades with higher axial induction near the root. For such rotors, the nacelle wake centre manifests as a velocity minimum.

In addition to dominating the mean flow features in the inboard region of the near wake, the nacelle is responsible for the generation of dynamical features, such as the hub vortex. The hub vortex has been described as a coherent structure that emerges from the hub as it convects downstream, it becomes unstable, expands radially and interacts with the tip vortices, influencing wake breakdown [9, 11]. The implications of this interaction for far wakes and farm aerodynamics are discussed below.

In the *far wake*, the effect of the support structure on the mean flow of a wind turbine was studied among others by Santoni et al. [12]. The inclusion of the support structure in their actuator line method large eddy simulations (ALM-LES) increased momentum entrainment and led to quicker recovery in the far wake. Therefore, when the support structure is simulated, a hypothetical downstream rotor in tandem may experience higher power availability than without the support structure being present. On the contrary, not simulating the support structure created a jet through the middle of the wake that stabilised the wake.

The low-frequency motion of the rotor far wake, known as wake meandering, affects both the overall farm power and dynamic loads experienced by downstream turbines in wind farms. Its origin and magnitude is still under discussion [11]. Among other phenomena, authors have observed that the interaction of the precessing hub vortex with the tip shear layer enhances the intensity of wake meandering [8, 9].

Wind farm aerodynamics are also influenced by the turbine's support structures. Ma et al. [13] identified that for high-density wind farms, the optimal rotor thrust reduces and therefore the relative importance of the tower increases. Incorporating the tower thrust within the momentum balance of a two-scale model showed that optimal wind turbine spacing in infinite and very large wind farms is affected by the tower thrust. Support structure considerations may therefore affect the design of large wind farms.

Stevens et al. [14] also found that the inclusion of a tower and nacelle model in actuator disc method (ADM) and ALM wind farm simulations improved mean flow predictions compared with experimental data. Specifically, higher turbulence and velocity deficit directly downstream of the turbines at various rows were observed.

The effect of the hub vortex on large wind farms was also assessed by Foti et al. [15]. In their work, a large wind farm excluding and including a nacelle model was simulated using actuator surface method (ASM) LES. Including a nacelle model increased the meandering amplitudes across the wind farm and especially in the first rows when compared with farm flow without a nacelle model. This is due to the interaction of the hub vortex with the tip shear layer that energises the wake, promotes turbulence generation and enhances wake meandering.

The vast majority of the above conclusions have been drawn from simulation data. However, the type of numerical model used to represent the support structure may vary significantly between simulations. Due to the multiscale and non-trivial interaction of wind rotors and their support structures, it is important to better

understand the sensitivity of the predicted flow to the chosen parameterisation of the tower and nacelle. To date, the trade-offs associated with various support structure modelling methods remain unclear, as comprehensive comparative studies on the subject are still limited.

In this paper, we are comparing computational fluid dynamics (CFD) methods from three different modelling families. First, a coarse mesh representation is employed, where the tower and nacelle are explicitly meshed; second, a meshless direct forcing cell-blocking method is tested, introduced by Apsley et al. [16] for the modelling of support structures of tidal rotors; finally, the widely used combination of an actuator disc (AD) representation for the nacelle alongside an actuator line (AL) with a prescribed Strouhal frequency for the tower is assessed. The methods are compared for their ability to replicate the near wake asymmetries that were observed in experimental measurements of the NTNU Blind Test 1 rotor wake. The analysis is carried out up to the far wake, where significant wake asymmetry is observed. The support structure modelling method that best represents experimental data is further employed to assess the influence of the tower when enhanced background turbulence levels are present.

The rest of this paper is structured as follows. In Section 2, the ALM-LES numerical method is briefly described. The three support structure modelling methods are discussed in Section 3. A comparison of the methods under low-background turbulence is presented in Section 4: Seven simulations are performed with different combinations of nacelle and tower configurations in order to better understand both the influence of the modelling method of the support structure of the flow prediction and the overall influence of the support structure in the physics of a wind turbine wake. The simulations employ low turbulence ($TI = 0.3\%$) to replicate the conditions of the blind test experiments that act as ground truth. The effect of enhanced background turbulence ($TI = 5\%, 10\%$) on the rotor/tower wake interaction is subsequently explored in Section 5. Conclusions are summarised in Section 6.

2 | Flow Solver and Rotor Parameterisation

In this work, an ALM embedded in an LES solver is employed for the prediction of the flow downstream of the NTNU rotor [17]. In what follows, a brief description of the NTNU Blind Test 1, the specifics of the LES solver and the parameters of the ALM are described.

2.1 | Experimental Dataset

The experimental dataset [17] used for comparison in this paper is that of the NTNU Blind Test 1. The NTNU rotor has a diameter of $D = 0.894$ m and its blades consist of the NREL S826 aerofoil along the entire span. The wind tunnel dimensions are $(L \times W \times H) = (11.15 \times 2.7 \times 1.826)$ m or $(12.47 \times 3 \times 2)D$ (Figure 1), and the rotor is centred at a hub height $z_h = 0.817$ m above ground. This configuration gives a blockage ratio of 12%. The freestream velocity at the inlet is $U = 10$ m/s, and the turbulence intensity at the rotor plane is $TI = 0.3\%$. The available experimental dataset consists of, among others, horizontal and vertical profiles of mean flow statistics at $x/D = 1$, 3 and 5 downstream of the rotor. In this paper, only a tip-speed ratio of $\lambda = 6$ is analysed. The nature of the interaction between the rotor wake and the tower wake may differ significantly for different tip speeds as a result of the thrust of the rotor being different. The influence of the support structure on the wake of the NTNU rotor at two different tip-speed ratios has been studied in other works [12].

2.2 | Numerical Scheme

The filtered, unsteady, incompressible 3D Navier–Stokes equations are solved using OpenFOAM [18] Version 2006. Second-order centred spatial and second-order backward temporal discretisation schemes are used, as is the PISO algorithm for the pressure–velocity coupling. The choice of subgrid-scale turbulence model does not generally affect the ALM-LES predictions of wind turbine wakes, as long as the simulation is sufficiently

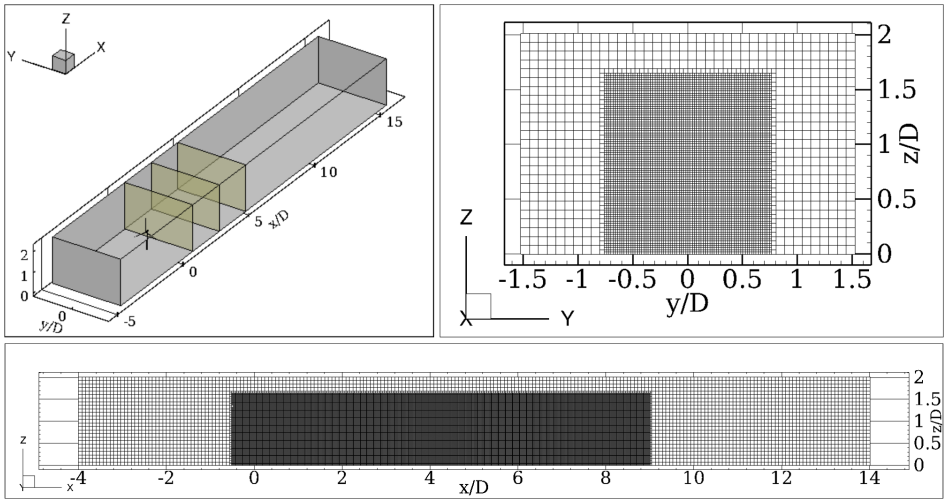

FIGURE 1 | Three-dimensional schematic of the domain and mesh topology for the simulations of the NTNU Blind Test 1. The rotor centre is located at $(x, y, z) = (0, 0, 0.8)$ m. The refined regions employ a refinement of N_x cells per rotor diameter.

well refined [19]. Therefore, the standard Smagorinsky turbulence model is employed.

The wind tunnel walls are modelled using a symmetry boundary condition. Synthetic eddies are superimposed in the inflow using the DFSEM method by Poletto et al. [20], available in OpenFOAM. A target turbulence intensity at the rotor plane and wake region is achieved by simulating the numerical wind tunnel without the turbine and measuring turbulence quantities at the locations of interest.

2.3 | Rotor Parameterisation

The LES-embedded ALM used in this study was adapted from SOWFA [21], validated by Wimshurst [22] and later transferred to OpenFOAM Version 2006. The blade is first discretised into a number of collocation points, and the ALM [23] is responsible for calculating the sectional blade forces at each collocation point. The ALM algorithm consists of three conceptual steps: the *flow sampling*, responsible for obtaining a two-dimensional incident velocity vector from sampling the three-dimensional CFD velocity field; the *force calculation*, where the forces at each blade section are calculated and three-dimensional flow corrections are imposed where relevant; and the *force imposition*, where a three-dimensional kernel is typically used to apply and smear out the calculated force back onto the CFD flow field.

The ALM parameters are chosen as follows in this study: 100 collocation points are used per blade, distributed cosinusoidally with a concentration of points at the root and tip. The largest distance between collocation points, at the middle of the blade span, is smaller than the local cell size, Δx, ensuring that the kernels always overlap, a necessary condition to establish a continuous load distribution and independence of the ALM solution from the number of collocation points.

The flow is sampled using the line average sampling method introduced by Jost et al. [24] and adapted for the ALM of horizontal axis wind turbines [25]. The method samples the flow at N points along a circular path of radius r_s, around the collocation point. Here, $N = 16$ sampling points are employed for each blade section placed at a sampling distance of $r_s = 1.1 r_g$ from the collocation point, where $r_g = 3\epsilon$ is the smearing radius of the force smearing kernel. Justification for the above parameter selection, alongside the description of the line average sampling method and a demonstration of its advanced numerical properties, is described in Zormpa et al. [25].

After sampling the local velocity magnitude and flow angle, the local blade forces are calculated at each collocation point. The lift and drag coefficient curves by Sarlak [26] are used, experimentally measured for a range of Reynolds numbers for the NREL S826 aerofoil. An anisotropic tip correction by Wimshurst and Willden [27] is also employed to account for three-dimensional effects near the tip that reduce the blade loads.

The ALM force is imposed back to the flow as a source term in the momentum equation. The calculated force is smeared using a commonly used three-dimensional isotropic Gaussian force kernel [23, 28, 29]. The smearing radius, $r_g = 3\epsilon$, is set using a typical value [29, 30] of $\epsilon = 2\Delta x$.

2.4 | Domain Size, Cell Size and Time Step

The CFD domain follows the dimensions of the wind tunnel. The mesh consists of hexahedral elements that gradually halve in size until they reach the most refined level that extends across the range $[x_{min}, y_{min}, z_{min}] = [-0.5D, -0.75D, 0]$ to $[x_{max}, y_{max}, z_{max}] = [9D, 0.75D, z_h + 0.75D]$ as can be seen in Figure 1. The cell size at the refined region corresponds to 100 cells per rotor diameter, that is, $N_x = D/\Delta x = 100$, where Δx is the side of the cubic cell. To assess the quality of the LES simulation, the turbulent kinetic energy ratio $\gamma = k_{res}/(k_{res} + k_{sgs})$ (where k_{res} is the resolved and k_{sgs} the subgrid-scale turbulent kinetic energy) has been calculated in previous verification studies [31]. It was found that $\gamma > 80\,\%$ for most regions of the far wake, with the exception of the tip vortices at the very near wake ($x/D \leq 1$) where $\gamma \approx 60\,\%$. This suggests satisfactory resolution for the ALM-LES, as the requirement for a well resolved LES is $\gamma > 80\,\%$ [32, 33], while lower values characterise a very large eddy simulation. A cell size of the order of $N_x = 100$ is commonly used in ALM-LES simulations of wind turbine wakes [19, 28, 29, 34].

Finally, the employed time-step size used in this work corresponds to 160 time steps per rotor rotation (i.e., $N_t = T/\Delta t = 160$) that has been found to provide robust rotor loads predictions when employing the line average sampling method [25].

3 | Support Structure Modelling Methods

Low-fidelity approaches are typically employed to model the support structure in ALM-LES simulations of wind turbine wakes for several reasons. Firstly, the wind turbine wake problem already consists of many scales requiring levels of numerical resolution that stretches the computational cost towards the upper limit of the available resources for many practitioners. Additionally, the problem of calculating the forces and wake of a support structure is that of a bluff body flow problem in transitional or supercritical Reynolds numbers that in itself is a resource-intensive CFD problem. Adequately resolving both the support structure and the far wake is expensive and impractical. Furthermore, even if the support structure is adequately resolved, uncertainty exists when it comes to roughness or other geometrical details of utility-scale flow towers in such high Reynolds number flows. Finally, the blades, arguably a more important contributor to the wake flow, are represented using a lower fidelity AL representation, and therefore, the same principle may also reasonably be applied to the support structure modelling.

Various methods have been used in the literature to model support structures. Some of the most common methods will be discussed below, starting with the higher fidelity parameterisation methods that involve limited assumptions and ending with representations that require predefining metrics related to the support structure forces.

Among the most accurate but also computationally expensive ways to simulate support structures is to explicitly mesh the solid boundary, using either a no-slip boundary condition with $y^+ \sim 1$ or a wall function with the first cell located in the log-law region. In the work of Muchala and Willden [35], URANS with a boundary-layer resolved tower and nacelle was employed, while in the work of de Oliveira et al. [36], a wall function approach was preferred. In the work of Ma et al. [37], a detached delayed eddy simulation (DDES) was chosen as the wall-modelled LES (WMLES) approach.

Immersed-boundary methods (IBMs) offer a meshless alternative to solid boundary modelling, avoiding the excessive meshing effort typically associated with the latter. These methods represent the presence of the modelled structure by adding a source term in the momentum equations. Many studies [6, 12, 38] employ an IBM implementation based on that of Orlandi and Leonardi [39]. Apsley et al. [16] modelled the support structures of tidal turbines using an alternative momentum source approach: In their implementation, the solid boundary is represented by means of adding a large source term in the momentum equations that drives the velocity locally to zero, effectively blocking the flow entering the volume occupied by the solid boundary. An implementation of this method, hereafter referred to as the cell-blocking method, is tested in the subsequent sections for the prediction of the mean flow downstream of a wind turbine with support structure.

Yang and Sotiropoulos [40] developed the ASM for both the modelling of wind turbine blades and the nacelle within LES simulations. The ASM generally explicitly considers more geometrical aspects than other actuator methods, such as the ALM. When employing the ASM for the nacelle, two forces are calculated and applied using a delta function at each location occupied by the boundary of the nacelle: the normal force, ensuring no-penetration and the tangential force, calculated using an empirical friction coefficient formula and information from the upstream flow.

Consistent with the blade modelling in ALM-LES simulations, towers and nacelles are often modelled using the AL and disc method, respectively [14, 19, 41–44]. For both components, a drag coefficient corresponding to that of a cylinder or disc is predefined and a characteristic inflow velocity vector has to be attained by sampling the surrounding flow. Sarlak et al. [19] further employed a predefined lift coefficient alongside a Strouhal frequency to introduce unsteadiness when modelling the tower of a model rotor; the inclusion of unsteadiness using such approaches has been subsequently employed in other validation studies [42, 43]. Other extensions to the actuator representations of the tower involve considerations of the pressure distribution around the surface of the tower [44].

While all of the above methods have been compared against experimental data or high-fidelity simulation results, little work exists in comparing methods with each other and understanding the trade-offs between them. Churchfield et al. [44] performed a comparison of various actuator methods for the support structure modelling and concluded that the standard ALM requires modification for the application in bluff bodies such as towers and nacelles.

In what follows, three support structure modelling methods are discussed: a body-fitted approach; a cell-blocking momentum source approach, following Apsley et al. [16]; and an AD/AL approach, following Sarlak et al. [19]. Schematic representations of the three methods are illustrated in Figure 2.

All three approaches are classified as low fidelity in the context of bluff body flows, and therefore, near wake predictions of the independent bluff bodies will not be studied. Instead, the methods are assessed based on their ability to interact correctly with the rotor wake. This is determined by evaluating the capability of each method to reproduce features observed in the experimental measurements of the NTNU rotor wake.

Finally, it is important to note that the accuracy of each support structure modelling method will depend on its own model parameters. In this work, the parameters of all methods are set as recommended from the literature in order to get a first idea of their performance when employed as intended. The self-convergence of each method may be studied in future work and informed by the

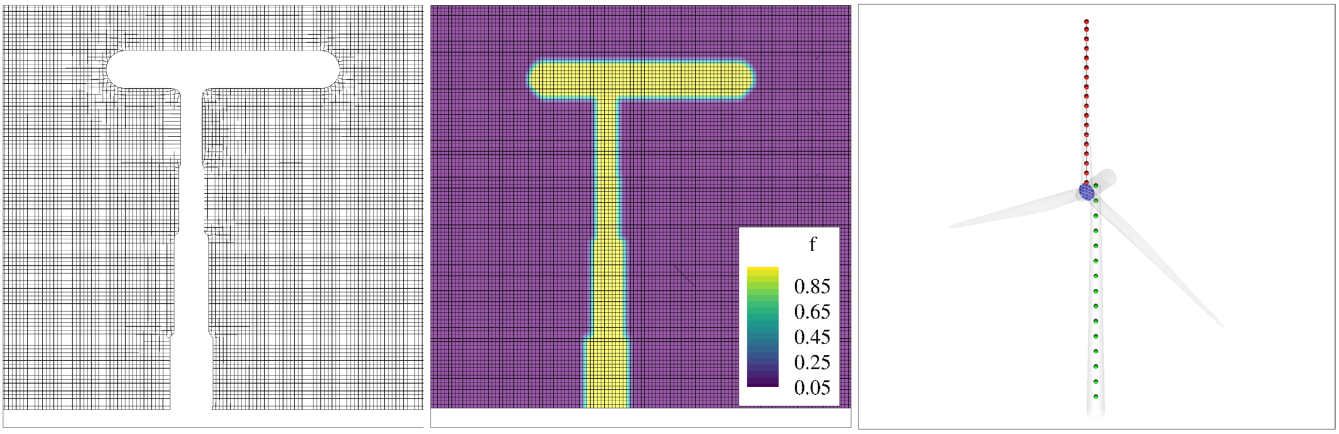

FIGURE 2 | Illustrations of three support structure parameterisation methods used in ALM-LES simulations. Left panel: a body-fitted mesh around a support structure; middle panel: the f field used by the cell-blocking method (Equation 3) to enforce the no-penetration of mass flow imposed by the no-penetration source term; right panel: schematic of the AD/AL representation. The tower is represented by the green collocation points, the nacelle by the blue AD and the blades by the red collocation points.

present study. The cell size at the support structure region is kept at $N_x = 100$ in order to allow for a fair comparison of the methods when no significant extra cost is introduced to model the support structure. That way we make our study relevant for simulations of multiple turbines or even ALM-LES modelling of wind farms.

3.1 | Body-Fitted Mesh: Geometry, Meshing and Boundary Conditions

The geometry of the tower simulated here has been sketched in Figure 3, following [45]. The dimensions of the tower and nacelle are kept close to these given in the report, but adjustments such as fillets between the different tower sections were added to facilitate meshing. The hub height is $z_h = 0.807$ m, $\sim 1\%$ shorter than described in [45], and the average tower diameter is $\overline{D}_{tow} = 0.075$ m, while the nacelle diameter is $D_{nac} = 0.09$ m.

The computational domain employed is described in Section 2 and employs $N_x = 100$. The support structure has been meshed by snapping hexahedral elements onto the solid boundary (Figure 2), using existing meshing tools available in OpenFOAM [46]. No additional refinement near the tower has been employed to ensure that the first cell remains in the log-law region. The y^+ was calculated at the last time step and was found to be in the range of $20 < y^+ < 300$. The employed cell size corresponds to $\overline{D}_{tow}/\Delta x \approx 8$ and $D_{nac}/\Delta x \approx 10$.

The support structure walls are modelled using an analytical shear stress wall function, based on the law of the wall. Studies such as [47, 48] have demonstrated that analytical wall-modelled LES approaches can provide good accuracy at a low cost. Other numerical details of the simulation have been summarised in Section 2.

The wake of a cylinder flow at subcritical Reynolds numbers, such as those experienced by the NTNU support structure, is separated and turbulent; therefore, a large number of cells are required to fully resolve the majority of scales using LES. Here, eight cells across the average tower diameter and 10 cells across the nacelle diameter are employed uniformly around and downstream of the support structure. Although the dynamics in the near wake of the support structure are not expected to fully converge, the primary focus here is on the interaction of the support structure with the rotor wake. Comparable mesh refinement levels have been used in similar works, for example, in Yang and Sotiropoulos [40], the velocity deficit and the dynamics downstream of a hydrokinetic turbine including the nacelle (represented by an ASM) were accurately captured using a mesh with $D_{nac}/\Delta x = 8$ ($D_{nac} = 0.08$ m, $\Delta x = 0.01$ m).

Employing the above numerical set up ensures that the cost of the ALM-LES simulation is not overtaken by the resolution requirements of the support structure.

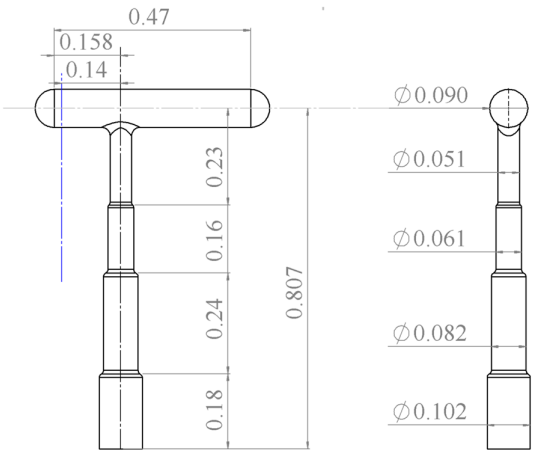

FIGURE 3 | Dimensions of the NTNU rotor's support structure simulated in this work. The design generally follows that of BT1 [45].

3.2 | Cell-Blocking Representation

The cell-blocking method was introduced in Apsley et al. [16] as a flexible method to model support structures of tidal rotors. It has been used in various tidal rotor simulations [16, 49, 50]. The method employs a momentum source term that is non-zero only within the cells occupied by the support structure. Its value is large enough to effectively block the mass flux from entering into a computational cell, acting as a nonpenetration condition.

Once discretised, the ith direction momentum equation in matrix form reads

$$Au = b \Rightarrow \alpha_P u_P - \Sigma_F \alpha_F u_F = b_P, \tag{1}$$

where A is the discretisation matrix, b is the source vector and u is the ith velocity component vector. Au can be further separated into the diagonal and nondiagonal parts, with corresponding subscripts $_P$ and $_F$, respectively. By adding an implicit source term $s_P u_P$, the diagonal of matrix A is artificially altered, and control over u_P can be obtained:

$$(\alpha_P - s_P)u_P - \Sigma_F \alpha_F u_F = b_P. \tag{2}$$

Setting $s_P \to \infty$ is balanced by $u_P \to 0$ so that a no-penetration condition can be enforced at the P^{th} cell. s_P needs to be infinite only in the numerical sense, and an appropriate value can be found by dimensional analysis. Equation (2) terms are expressed in Newtons. Therefore, s_P can be expressed as [16]

$$s_P = -f\rho\frac{u^*}{L}V_P, \tag{3}$$

where f takes values of $f \in (0, 1)$ (Figure 2) and represents the volume fraction calculated as the volumetric proportion of the cell that is occupied by the solid. ρ is the fluid density; u^* represents a large velocity value that is taken as 10 times the inflow speed, larger than any velocity anticipated within the domain; and L is the characteristic cell length taken as $V_{ave}^{1/3}$, where V_{ave} is the average cell volume.

Due to its implementation as an implicit source term, the cell-blocking technique lacks a wall treatment, often considered in immersed-boundary approaches. Given that the typical cell size in ALM-LES simulations does not resolve the inner layer, a large boundary layer that scales with the mesh size has been observed to emerge from solid boundaries represented using the cell-blocking method, resulting in an overprediction of the body force as a result.

Finer meshes yield thinner boundary layers and a more realistic body force. The objective of the current study is to evaluate the ability of the tested methods to improve the wake predictions without increasing the computational expense. Therefore, the mesh here was not refined to accommodate a better prediction of the support structure force. Another argument against attempting mesh refinement is that achieving satisfactory agreement with a canonical cylinder flow using a cell-blocking model at such Reynolds numbers is computationally virtually impossible requiring DNS level resolution and case specific. The significance of spurious features such as the thick boundary layer is tested in the context of wind turbine wakes in the following sections.

3.3 | AD/AL Representation

In this approach, the nacelle is represented using an AD and the tower using an AL, a widely used approach for the modelling of the support structure [19, 42, 44]. Such AD/AL approaches have been demonstrated to improve wake predictions of the NTNU rotor [43].

3.3.1 | ADM Nacelle Modelling

For the nacelle, an AD approach may be employed to limit the flow through the centre of the rotor. Here, the variable-scaling ADM [51] is used, as implemented in OpenFOAM Version 2.2.0 and above [52]. The method uniformly imposes a thrust force of magnitude

$$T = \frac{1}{2}\rho|\mathbf{u_0}\cdot\mathbf{n}|^2 A C_T^*, \tag{4}$$

and direction $\mathbf{n}$, where $\mathbf{n}$ is the unit vector normal to the AD surface A. C_T^* is the calibrated thrust coefficient

$$C_T^* = C_T\left(\frac{|\mathbf{u}_m|}{|\mathbf{u}_0|}\right)^2, \tag{5}$$

introduced to account for the deceleration of the upstream flow. C_T is the user-defined thrust coefficient, based on a freestream velocity measurement and $\mathbf{u}_m$ is the freestream velocity sampled at a user-defined monitoring point m. The user-defined parameters in this method are therefore the thrust coefficient C_T and the location of the monitoring point m.

In the absence of a reference drag coefficient for the nacelle, the thrust coefficient for the following simulations is calculated using the body-fitted simulation results. In order to impose a constant thrust, the monitoring point is placed at the disc centre such that $\mathbf{u}_m \approx \mathbf{u}_0$. Then, C_T is calculated such that the AD force is the same as the body-fitted nacelle force.

3.3.2 | ALM Tower Modelling

The tower is modelled using the ALM along its length, with a constant drag component and a fluctuating lift component, following Sarlak et al. [19]. All parameters here are taken from the same publication [19] that used this approach for the NTNU rotor. Other works have also utilised the same method and parameters to model the NTNU turbine tower [42, 43].

The drag coefficient is set to $C_D = 1.2$, following measurements on cylinders from subcritical up to transcritical Reynolds numbers [53]. The dynamic lift coefficient is expressed as

$$C_L(t) = a\ \sin(2\pi f t) + B(t). \tag{6}$$

The Strouhal number is set to $St = fD/U = 0.2$, where D is the tower diameter, U is the inflow velocity and f is the frequency of the lift force fluctuation in Hz. The root mean square of the lift coefficient is set to $a = 0.3$, representative of cylinder flows in similar Reynolds numbers. White noise, $B(t)$, with standard deviation $\sigma = 0.25C_L$ is used to introduce random perturbations that mimic turbulent fluctuations in the shedding process.

The parameters of the ALM are chosen as follows. The flow is sampled at each collocation point and the lift coefficient frequency is calculated through the Strouhal number using the local tower diameter. The force is imposed by means of a spherical Gaussian kernel with a smearing value of $\varepsilon = 2\Delta x$. This gives $\varepsilon/D_{tower} \approx 0.25$, which is close to the optimal recommended value by Martínez-Tossas et al. [54]; however, this value is calibrated for potential flow. Further works by Rocchio et al. [55] have demonstrated that the ALM experiences shortcomings in separated flows and propose a smaller value of ε. However, here the aim is to fairly compare all support structure modelling methods without adding to the computational cost of a standard ALM-LES wake simulation, which is why ε is not adjusted further.

Both the cell-blocking and AD/AL methods are meshless representations that employ momentum sources to model solid objects. However, they are based on fundamentally different principles. The cell-blocking method explicitly represents the geometry by imposing a numerically large momentum source within the cells occupied by the solid body, effectively enforcing a no-penetration condition. This approach requires definition of the body's geometry however is agnostic of the resultant body force. On the other hand, the actuator method prescribes body forces based on predefined coefficients and simulation of the exact geometry of the solid boundary is not required.

4 | Results: Low-Background Turbulence

The support structure modelling methods reviewed in Section 3 are compared in this section. In order use the NTNU Blind Test 1 experimental measurements as ground truth, all simulations of this section employ a rotor plane background turbulence intensity of $TI = 0.3\%$. Background turbulence is expected to influence the degree at which the rotor wake interacts with the support structure wake and therefore simulation results at higher background turbulence levels are discussed in Section 5.

4.1 | Simulation Suite

The three modelling methods described in the previous section are applied for the modelling of the support structure of the NTNU rotor. Seven simulations are performed, listed in Table 1.

The nomenclature for each case consists of two words separated by a hyphen: the first refers to the nacelle and the second one to the tower modelling method. 'MSH' corresponds to body-fitted modelling of the support structure component, 'CB' corresponds to cell blocking, 'AD' to actuator disc nacelle representation and 'AL' to actuator line tower representation. 'X' denotes that the structural component is not modelled.

4.2 | Rotor and Support Structure Forces

The axial force on the nacelle ($F_{ax,nac}$), tower ($F_{ax,tow}$) and combined support structure ($F_{ax,ss}$) as well as the thrust of the rotor ($F_{ax,rot}$) for each simulated case of Table 1 are presented in Table 2. Reported values have been averaged across the last five rotor rotations, to capture the mean effect of the turbine dynamics and turbulence. While the forces in the MSH cases are calculated by summing the viscous and pressure forces, in the CB and actuator cases, they are calculated as the sum of the momentum source at each cell.

The diameter-based Reynolds number of the nacelle, using the freestream velocity $U_\infty = 10$ m/s, is $\mathrm{Re}_{nac} = 5\times10^4$. The axial force calculated using MSH-X is $F_{ax,nac}^{MSH-X} = 0.29$ N. This gives an overall drag coefficient of $C_D = 0.74$ for the nacelle, and the ratio between the rotor thrust and nacelle drag is $F_{ax,rot}/F_{ax,nac}^{MSH-X} \approx 113$. The CB-X simulation applies a nacelle drag force ~ 1.5 times larger, which is likely related to the thick boundary layer produced by the method due to the lack of wall treatment and consequent increase in momentum deficit. The thrust coefficient for the AD-X method has been calculated based on MSH-X, and therefore, the force is the same as $F_{ax,nac}^{MSH-X}$. In all three nacelle-only cases, the presence of the nacelle contributes to a slight increase in rotor thrust when compared with the X-X case due to diversion of flow around the hub towards the inner sections of the blades.

TABLE 1 | Summary of the support structure simulations performed alongside the nomenclature used to indicate the nacelle and tower modelling methods.

Nacelle modelling	Tower modelling	Label
None	None	X-X
Mesh	None	MSH-X
Mesh	Mesh	MSH-MSH
Cell blocking	None	CB-X
Cell blocking	Cell blocking	CB-CB
Actuator disc	None	AD-X
Actuator disc	Actuator line	AD-AL

The Reynolds number based on the average tower diameter $\overline{D}_{tow}$ and freestream velocity $U_\infty = 10$ m/s, is $\mathrm{Re}_{tow} = 4.2\times10^4$. An approximation of the force experienced by the tower component only can be given by $F_{ax,tow} = F_{ax,ss}^{MSH-MSH} - F_{ax,nac}^{MSH-X} = 1.3$ N, giving a $C_D = 0.35$ and $F_{ax,rot}/F_{ax,tow} = 25$.

The support structure force predicted by the cell-blocking method is approximately 2.1 times larger than the body-fit force. The AD-AL support structure force is 0.75 of $F_{ax,ss}^{MSH-MSH}$.

Pierella and Sætern [5] discuss the rotor to tower axial force ratio, $F_{ax,rot}/F_{ax,tow}$. For the NTNU rotor, alongside the rotor thrust they assumed a tower coefficient drag coefficient of $C_D = 1.2$ giving $F_{ax,rot}/F_{ax,tow} = 7$ for specified operating conditions. Here, a smaller tower drag is calculated using body-fitted simulations, giving a ratio $F_{ax,rot}/F_{ax,tow} = 25$. This ratio is closer to the ratio predicted by Pierella and Sætern for a utility-scale rotor: the rotor to tower thrust ratio for the DTU 10-MW rotor, assuming a tower drag coefficient of $C_D = 0.7$ is estimated as $F_{ax,rot}/F_{ax,tow} = 39$. This might suggest that the analysis here might be relevant for utility-scale rotor. However, such approximations are likely unreliable due to the dynamic upstream flow incident to the tower and the complex bluff body flow aerodynamics.

The body force prediction of the various methods considered has been estimated to vary by a maximum factor of 2.1. This difference stems from the different treatments inherent to different methods, the cell size and the user-defined values of various parameters. The variance of force predictions between methods is deemed reasonable when compared with the magnitude of the rotor thrust. In the absence of an accurate tower force estimate to be used as a baseline, the methods are employed with a recognised inconsistency in forces: the effect

TABLE 2 | Mean axial force values for the support structure components alongside the mean rotor thrust for the simulations of Table 1.

Simulation	Nacelle drag $F_{ax,nac}$ (N)	Tower drag $F_{ax,tow}$ (N)	Support structure drag $F_{ax,ss}$ (N)	Rotor thrust $F_{ax,rot}$ (N)
X-X	0	0	0	33.59
MSH-X	0.29	0	0.29	33.74
MSH-MSH	—	—	1.59	33.59
CB-X	0.49	0	0.49	33.71
CB-CB	—	—	3.45	33.43
AD-X	0.29	0	0.29	33.68
AD-AL	0.28	0.919	1.19	33.55

that the force may have on the wind turbine wake is considered part of the wake problem and is tested in the following sections.

4.3 | Instantaneous Flow

A qualitative comparison of the instantaneous vorticity magnitude of the wakes from each simulation of Table 1 is presented in Figure 4.

While root vortices can be identified in the X-X simulation, they are weakened or broken down in all other simulations.

The tip vortex breakdown in the tip region above hub height in the xz plane is consistent in all simulations and occurs at approximately $x/D = 1.5$. However, the tip vortices below hub height are strongly affected by the presence of the tower, leading to an immediate breakdown of the tip vortices that interact with it. This feature is less well captured in the AD-AL case, where tip vortical features below hub height persist after their interaction with the tower.

The region downstream of the tower for both MSH-MSH and CB-CB simulations is characterised by the strong presence of turbulent eddies. This is related to the ability of the two methods to promote flow separation downstream of the modelled tower,

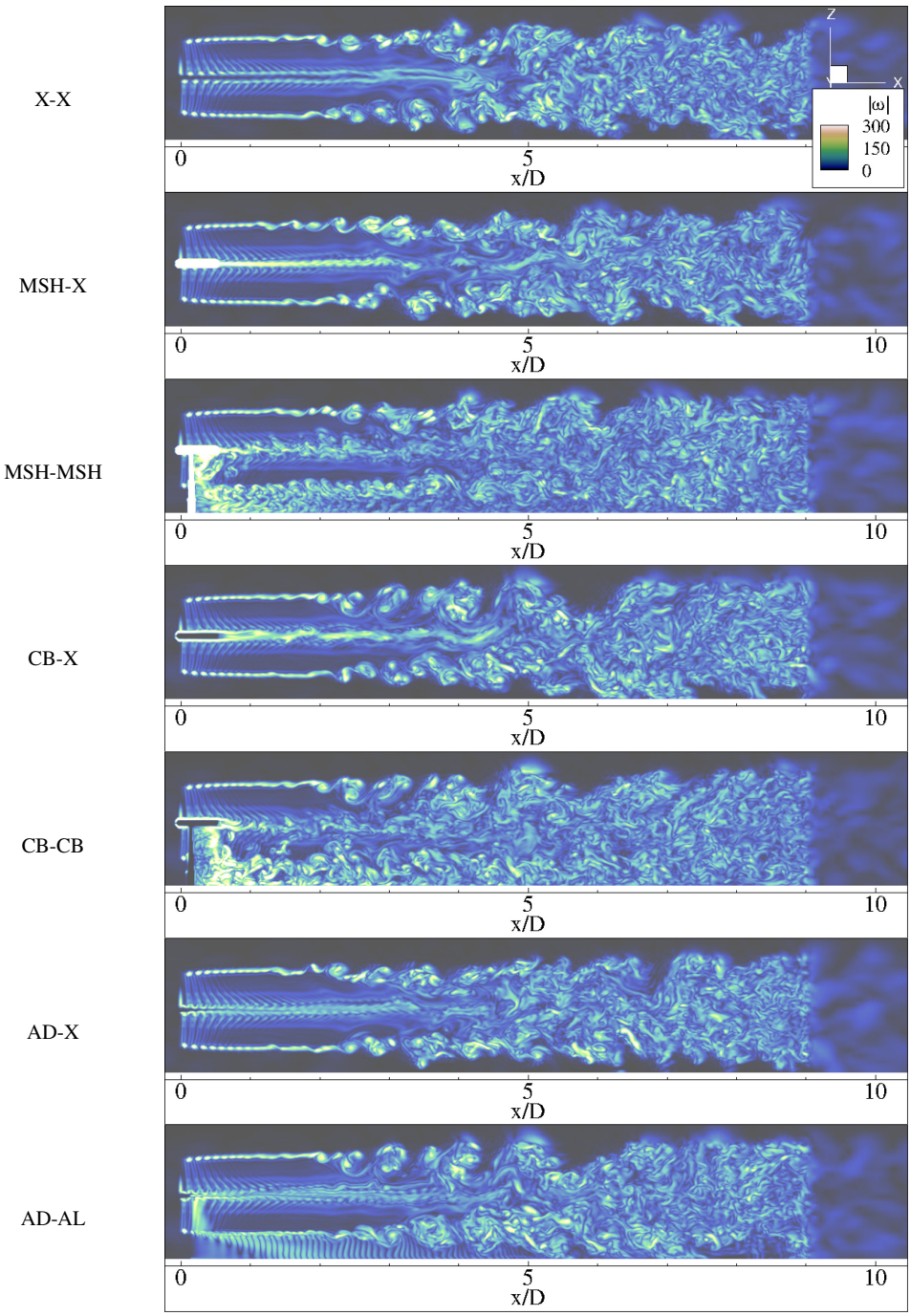

FIGURE 4 | Contours of instantaneous vorticity magnitude across a vertical plane through the centre of the rotors. See Table 1 for nomenclature.

generating a more realistic bluff body wake. In the AD-AL case, dynamic features can be observed in the lower part of the rotor wake and downstream of the tower as a result of the imposed dynamic lift described in Equation (6). However, these structures do not resemble turbulent eddies. This is likely linked to the inability of the ALM model to represent separated flows, [55], if the kernel size, ϵ, is not adjusted.

In the far wake, for example, at $x/D = 8$, the centreline and tip vorticity have merged into a seemingly homogeneous turbulent wake in all simulations. In the three tower cases, turbulent structures extend to the lower wall of the simulation ($z = 0$), while in the axisymmetric cases the wake has expanded at a similar rate below and above hub height.

4.4 | MSH-X and MSH-MSH: Support Structure Influence on Near Wake Predictions

The mean velocity and TKE profiles of simulations X-X, MSH-X and MSH-MSH are presented in both the horizontal and vertical planes in Figure 5, for three downstream locations x/D=1, 3 and 5. The effect of including first the nacelle and then the tower as meshed structures in ALM-LES simulations of wind turbine wakes is explored. Numerical predictions are compared with the measured experimental data of BT1.

Alongside the flow profiles, the interaction between the wake of the support structure and the wake of the rotor, captured in the MSH-MSH simulation is further explored. The evolution of the mean velocity and TKE contours in the near and far wake is visualised in Figure 6.

4.4.1 | Streamwise Location $x/D = 1$

The ALM-LES prediction of the horizontal and vertical mean flow profiles at $x/D = 1$ benefit significantly from the inclusion of both the tower and nacelle when compared with the experimental measurements.

The $-0.2 < y/R < 0.5$ inboard section of the wake, measured in the horizontal plane, is characterised by a peak in mean velocity deficit together with a peak in TKE (Figure 5a,c, $x/D = 1$). Both peaks correspond to the tower wake being swept upwards by the rotor wake, as observed in the $x/D = 1$ flow contours of Figure 6. This behaviour is accurately captured by the MSH-MSH simulation.

The mean flow prediction in the region below the lowest blade point, $(z - z_h)/R < -1$, visualised in the vertical profiles of Figure 5b,d, is somewhat improved when the MSH-MSH support structure representation is used: The presence of the tower

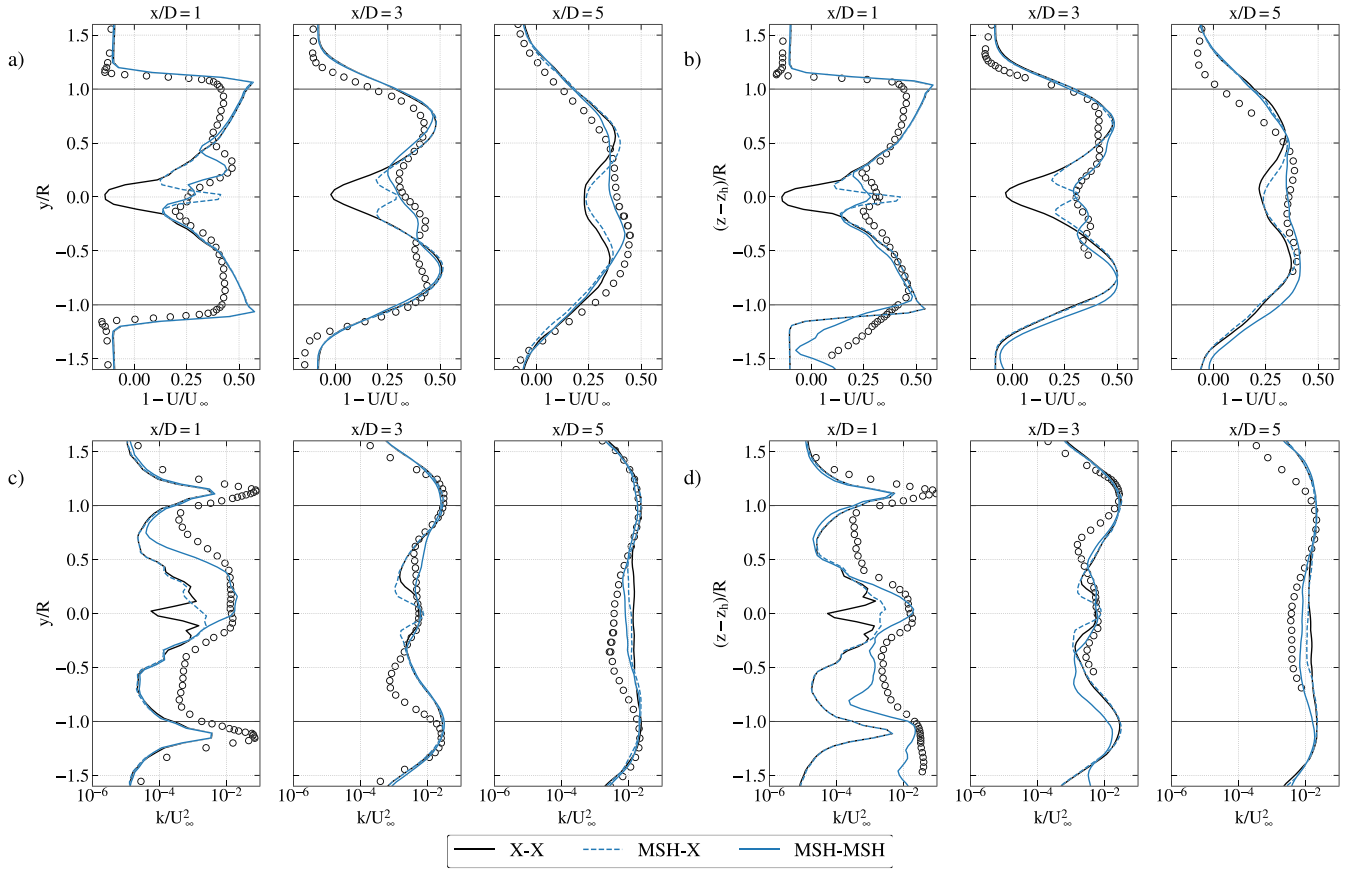

FIGURE 5 | Horizontal and vertical mean flow profiles downstream of the rotor plane for the body-fitted simulations summarised in Table 1, at downstream locations x/D=1, 3 and 5. (a) Horizontal plane mean velocity deficit, (b) vertical plane mean velocity deficit, (c) horizontal plane TKE and (d) vertical plane TKE. Black circles denote experimental measurements [17].

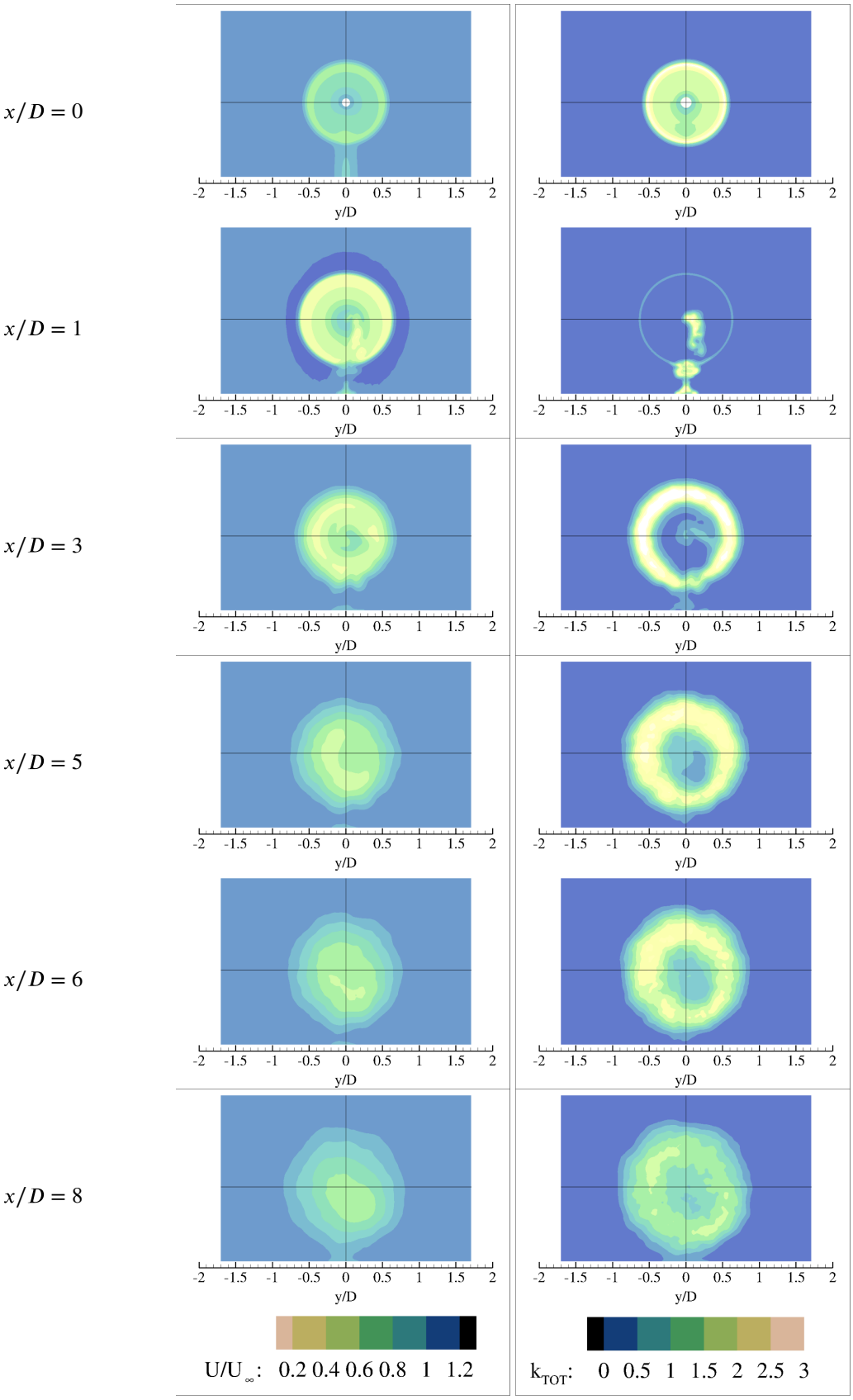

FIGURE 6 | MSH-MSH: Streamwise evolution of the mean velocity (left) and TKE (right) downstream of the rotor plane. Two-dimensional planes have been extracted at streamwise locations $x/D = 0$, 1, 3, 5, 6 and 8.

contributes to an increase in the velocity deficit and the TKE in these locations. However, the measured deficit on this lower side is still greater than that which was simulated.

The inclusion of the nacelle only (MSH-X) generally suppresses the spurious jet through the rotor centre and therefore improves the mean velocity and TKE prediction at $x/D = 1$ in comparison with the simulation without any support structure (X-X). However, the asymmetric features observed in the experimental measurements and closely matched by the MSH-MSH simulations are not captured by the MSH-X simulation, the wake of which remains axisymmetric.

All simulations of Table 1 consistently overpredict the momentum deficit at the edge of the wake, $|y/R| \approx 1$. This behaviour results from several compounding factors, such as the blockage of the domain, the low turbulence levels that allow the tip vortices to be more persistent and the choice of the Gaussian kernel width of the AL. Similar peaks at the edge of the near wake have been observed for the same rotor in other studies [34, 56]. Away from the overprediction of the momentum deficit at the edge of the near wake, the effect of the support structure can be identified in the inboard sections of the wake for all streamwise stations in the range $1 \leq x/D \leq 5$ (Figure 5).

Another aspect of the ALM that can be observed consistently for all simulations is the underprediction of blade-induced TKE, visible in the mid-span region of the TKE profiles of Figure 5b,d, $x/D = 1$). Similar behaviour is generally observed in most ALM near wake predictions [17].

4.4.2 | Streamwise Location $x/D = 3$

The mean velocity deficit predicted by the MSH-MSH simulation, sampled at the horizontal plane three diameters downstream of the rotor plane (Figure 5a,c, $x/D = 3$), also follows the experimental measurements closely. In both the experimental dataset and the MSH-MSH results, the local velocity deficit peak in the inboard section of the wake has switched side of the centreline when compared with its position at $x/D = 1$. This is attributed to the swirling of the tower wake by the rotor wake as visualised in the mean velocity contours $x/D=1$ and 3 of Figure 6. MSH-MSH predictions also follow closely the experimentally measured mean velocity deficit at the vertical plane (Figure 5b,d, $x/D = 3$).

Adding only a nacelle model (MSH-X) affects the wake at $x/D = 3$ in the same way that it does at $x/D = 1$: The spurious jet is suppressed, and as a result, MSH-X can predict wakes that are in better agreement with experimental measurements than the predictions of X-X simulation. However, nacelle-only methods are unable to predict the asymmetry introduced into the wake by the tower.

4.4.3 | Streamwise Location $x/D = 5$

At $x/D = 5$, the MSH-MSH simulations still outperform the other simulations in terms of agreement with the experimental measurements. The MSH-MSH wake follows closely the experimental data and presents asymmetric features. Mean flow profiles of X-X and MSH-X simulations are in close agreement, contrary to observations in upstream streamwise locations where MSH-X outperformed the X-X predictions by suppressing the spurious centreline jet behaviour.

The asymmetry observed in the flow profiles at this streamwise station can be explained by observing the three-dimensional evolution of the rotor wake. The TKE contours at $x/D = 1$ demonstrate an increased TKE levels at $(z - z_h)/R \approx -1$ and $r/R = 1$, as a result of the interaction between the tip vortices and the tower structure and wake. The sections of the rotor wake edge that have interacted with the tower develop less shear at $x/D = 2$ onwards compared with those that have not interacted with the tower. This imbalance is rotated by the rotor wake. The combined result of the interaction with the tower and the wake rotation leads to higher tip region turbulence in quadrant $y/R < 0, (z - z_h)/R > 0$ and lower tip turbulence in quadrant $y/R > 0, (z - z_h)/R < 0$ at downstream locations. This evolution explains the asymmetry observed in the experimental measurements and MSH-MSH predictions at $x/D = 5$.

The observation that satisfactory agreement with experiments at $x/D = 5$ can only be achieved by fully modelling the tower suggests that the influence of the tower persists into the far wake and is not insignificant compared with the rotor wake, even though the associated support structure may be small compared with the rotor. In the flow velocity contours of Figure 6, at $x/D = 8$, significant asymmetry has developed further downstream into the far wake that might result in differences with engineering models that employ the Gaussian far wake assumption.

The above flow contours and discussion also confirm and extend the work of Pierella and Sætran [5]. In their work, mean velocity contours of the same rotor were measured using a five-hole Pitot tube at locations $x/D=0.6$, 1, 1.5, 2 and 3. Observations allowed them to identify, among other features, a disruption in the azimuthal symmetry of momentum entrainment. Discussion here further explains the interaction between the support structure wake and the rotor wake by means of turbulence quantities. The extended available data range, up to $x/D = 8$, allows the study of the effect of the support structure in the far wake.

4.5 | Support Structure Modelling Method Effect on Wake Predictions

4.5.1 | Nacelle-Only Simulations

The effect of different nacelle modelling options is discussed in this section. Horizontal mean velocity and TKE predictions of the NTNU rotor are presented in Figure 7, respectively, for four downstream locations $x/D=1$, 3, 5 and 8. A comparison with experimental data is not performed, because a tower model is omitted in these simulations.

AD-X and MSH-X nacelle representations impose the same resistance to the flow given the axial force measurements presented in Table 2. This is also depicted by the close agreement of the methods in predicting the mean velocity deficit at all

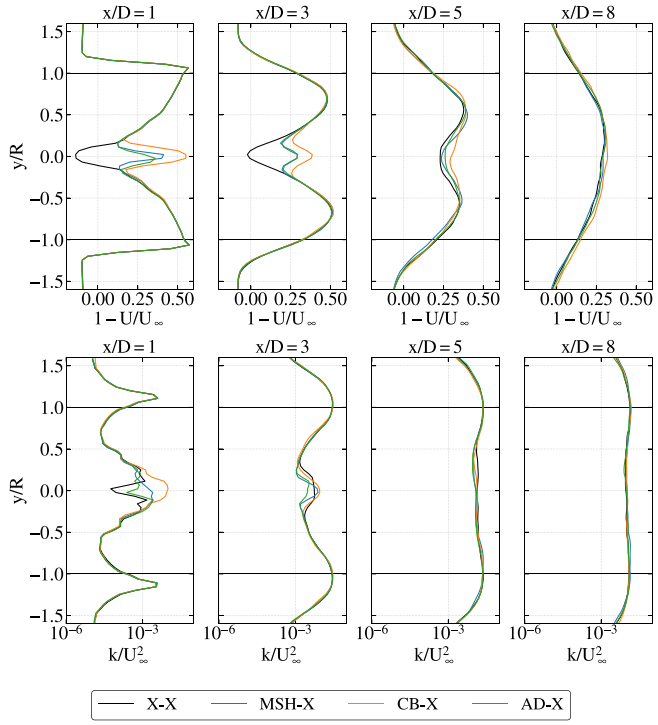

FIGURE 7 | Horizontal mean flow profiles downstream of the rotor plane for the nacelle-only simulations summarised in Table 1, at downstream locations $x/D=1$, 3, 5 and 8. Upper panel: non-dimensional mean velocity deficit profiles; lower panel: non-dimensional TKE profiles.

downstream locations of Figure 7. MSH-X introduces slightly higher TKE peaks owning to the ability of the body-fitted method to generate a separated flow.

CB-X imposes a large force in the flow and thus introduces a high velocity deficit accompanied by high TKE, at $x/D = 1$ when compared with the MSH-X simulation.

Regardless of the nacelle representation, all simulations predict similar mean flow profiles at $x/D = 8$ across the wake span suggesting that all methods might be appropriate for a nacelle-only representation if the focus is on the mean flow of the far wake.

4.5.2 | Nacelle and Tower Simulations

Having established that the MSH-MSH support structure model closely follows experimental measurements of the NTNU rotor near wake in Section 4.4, the capability of the CB-CB and AD-AL simulations to capture the same features is assessed. Horizontal profiles of the mean velocity deficit and TKE profiles at four downstream locations $x/D=1$, 3, 5 and 8 are presented against experimental measurements in Figure 8.

At $x/D = 1$, the peaks of mean velocity deficit and TKE at $-0.2 < y/R < 0.5$, identified as a result of the tower/rotor wakes interaction, are captured by both MSH-MSH and CB-CB methods. This is attributed to the ability of the two methods to generate a turbulent wake downstream of the tower that interacts with the rotating wake of the rotor. On the other hand, while the AD-AL simulation presents some asymmetry in the combined wake, the mean velocity and TKE profiles do not follow the experimental data.

At $x/D = 3$, both the CB-CB and AD-AL methods deviate from the experimental measurements. The mean velocity deficit peak at $y/R \approx -0.25$, observed in the experimental data, cannot be identified in the CB-CB mean velocity profiles, as the deficit appears to have mixed with the surrounding flow, as implied by the enhanced TKE at $x/D = 3$ as a result of the CB-CB implementation. The prediction of the AD-AL method presents a symmetric flow field, suggesting that the tower wake created by the AL was not sustained in the far wake of the turbine. This may be attributed to the lack of flow separation captured in the tower ALM if the model parameters are not properly calibrated, as discussed by Rocchio et al. [55].

At $x/D = 5$, the experimental measurements present a slightly higher velocity deficit around $y/R \approx -0.4$. Both MSH-MSH and CB-CB also capture this asymmetric behaviour. The AD-AL method improves the wake prediction at that streamwise station, when compared with the X-X case and the AD-X case (Figure 8). TKE predictions at $x/D = 5$ are slightly improved for all methods when compared with the X-X case.

At $x/D = 8$, the mean velocity deficit predictions for all simulations apart from CB-CB are in close agreement. The latter predicts significant asymmetry of the flow deficit at the horizontal plane due to a highly turbulent support structure wake caused by both a large body force and the lack of wall treatment within the cell-blocking technique.

The difference between simulations and experiments has been quantified for the velocity profiles presented in Figure 8. The ℓ^2 norm of the difference between the experimental ($\epsilon(y_i)$) and simulated ($s(y_i)$) mean velocity deficit ($1 - U/U_\infty$) is defined as $\ell^2 = \sqrt{\sum_{y_i=y_1=-1.5R}^{y_i=y_N=1.5R} (\epsilon(y_i) - s(y_i))^2}$, quantified for the three downstream locations where experimental measurements are available at hub height. The triplet $(\ell^2_{x/D=1}, \ell^2_{x/D=3}, \ell^2_{x/D=5})$ corresponding to each of the support structure modelling methods is found to be X-X: $(1.54, 1.27, 0.87)$, MSH-MSH: $(0.86, 0.62, 0.45)$, CB-CB: $(0.74, 0.57, 0.43)$ and AD-AL: $(1.01, 0.73, 0.60)$.

We note that the above error metrics have been calculated based on the available hub-height measurements and therefore are not fully representative of the three-dimensional wake flow. However, several observations can be made. First, the ℓ^2 norm decreases with distance from the rotor for all methods, suggesting that both the ALM and the support structure modelling methods tested in this work may be yield better performance for far wake predictions than near wakes. Second, at all streamwise locations, simulation X-X presents the largest ℓ^2 norm, followed by AD-AL. The MSH-MSH and CB-CB predict smaller ℓ^2 norms, outperforming the AD-AL and X-X methods. These results indicate that including even a simplified support structure representation leads to improved agreement

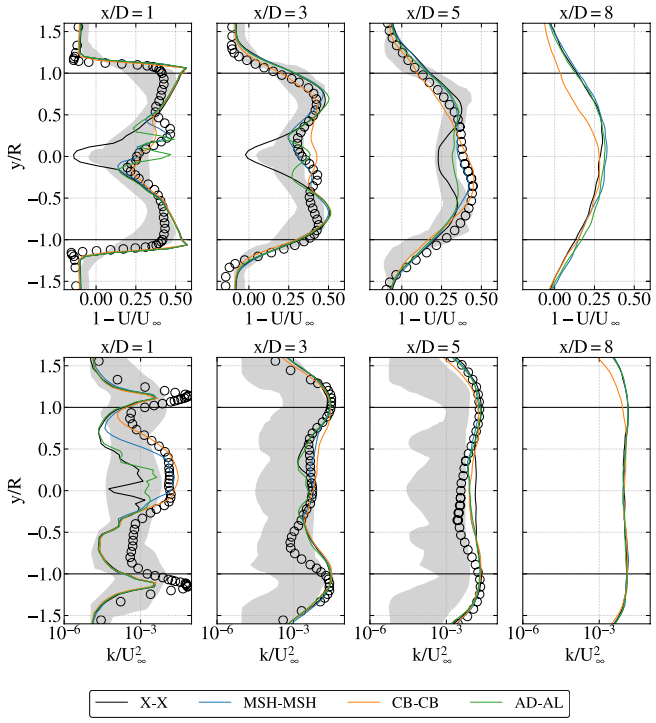

FIGURE 8 | Horizontal mean flow profiles downstream of the rotor plane for the nacelle-only simulations summarised in Table 1, at downstream locations $x/D=1$, 3, 5 and 8. Upper panel: non-dimensional mean velocity deficit profiles; lower panel: non-dimensional TKE profiles. Black circles denote experimental measurements and shaded areas correspond to the range of numerical predictions from various modelling methods [17].

between simulated wakes and those observed in wind tunnel experiments.

5 | Results: Enhanced Background Turbulence

The low-background turbulence conditions studied in the previous section are well suited for a comparison between support structure modelling methods, as they allow focus on the interaction between the support structure and turbine blades without exogenous disturbances in addition to the validation against experimental data. However, at the utility scale, high background turbulence is present which influences the interaction between the rotor and its support structure.

In this section, the effect of background turbulence intensity of the numerical wind tunnel is evaluated at 5% and 10% at the rotor plane. Turbine simulations without the nacelle or tower (X-X) are compared against simulations with meshed nacelle and tower (MSH-MSH). The latter method is selected as MSH-MSH presented satisfactory agreement with the experimental measurements of the NTNU Blind Test with low turbulence at all streamwise locations. The mean rotor thrust is in close agreement across all simulations which ensures that the mean wake flows in this section are comparable.

The mean velocity deficit at four downstream locations, and three turbulence levels is presented in Figure 9. Across all

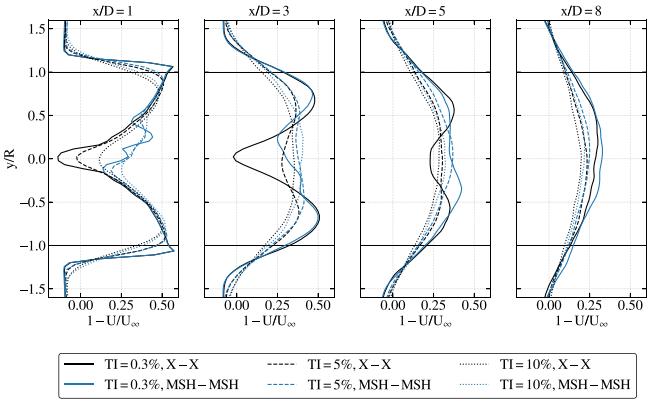

FIGURE 9 | Horizontal profiles of the non-dimensional mean velocity deficit downstream of the rotor plane at locations $x/D=1$, 3, 5 and 8 under the influence of increasing ambient turbulence intensity.

turbulence intensity levels simulated here, the influence of the support structure is dominant in the inboard sections of the near wake, that is, at $|y/D| < 0.5$ and $x/D = 1$. On the contrary, the flow close to the edge of the near wake, $|y/D| \approx 1$, is dominated by the background turbulence.

Higher turbulence contributes to reducing far wake asymmetries induced by the tower, visualised for the horizontal profiles of mean velocity deficit in Figure 9. The enhanced velocity deficit due to the presence of the support structure persists up to eight diameters downstream of the rotor. This indicates that while enhanced background turbulence acts more effectively to spread the wake momentum deficit, the wake deficit is not completely recovered by the enhanced turbulence.

To quantify the above, the ℓ^2 norm is redefined as $\ell^2 = \sqrt{\sum_{y_i=y_1=-1.5R}^{y_i=y_N=1.5R} (s_{X-X}(y_i) - s_{MSH-MSH}(y_i))^2}$ in order to calculate the quadruplet $(\ell^2_{x/D=1}, \ell^2_{x/D=3}, \ell^2_{x/D=5}, \ell^2_{x/D=8})$ that summarises the influence of the support structure at various downstream locations. ℓ^2 norm drops both with an increase in streamwise location and an increase in background turbulence, that is, $TI = 0.3\%$: (1.16, 0.99, 0.62, 0.25), $TI = 5\%$: (0.94, 0.45, 0.32, 0.16), $TI = 10\%$: (0.63, 0.32, 0.22, 0.20). These measures confirm that, moving downstream, the differences in the mean wake profile between cases where the support structure is and is not simulated are relatively small.

While increasing background turbulence reduces the importance of the support structure in the far wake, it is observed that the tower and nacelle still plays a major role in the near wake, even when turbulence intensity is 10%. The present simulations investigate the effect of elevated turbulence levels in otherwise uniform wind tunnel flow; other phenomena that occur in the real world such as a sheared velocity profile would also influence wake entrainment for utility-scale turbines; however, they are beyond the scope of the present study.

6 | Conclusion

In this work, aspects surrounding the interaction between support structures and wind turbine wakes were studied. Three

low-cost methods for representing the tower and nacelle were implemented and compared: a body-fitted method that uses an analytical wall function, a cell-blocking meshless forcing method and an AD/AL approach.

The body-fitted method was found to successfully generate a turbulent wake downstream of the tower and nacelle without significantly adding to the numerical cost of the ALM-LES simulation, despite the meshing requirement to model the structure. It was capable of capturing all asymmetric near wake features observed in BT1 measurements, without the need for user-defined parameters. Two significant consequences of the interaction between the support structure and the rotor wakes were identified: (i) a nonaxisymmetric flow in the inboard sections of the near wake and (ii) a tower-induced imbalance in the breakdown of tip vorticity that led to an asymmetry in the TKE in the outboard regions of the far wake. This in turn generated a nonaxisymmetric far wake velocity deficit characterised by a vertical drop in the wake centre.

The cell-blocking method, which does not require mesh modifications and is also free of user-defined tuning parameters, was capable of introducing a turbulent wake downstream of the support structure, correctly capturing many nonaxisymmetric aspects of the interaction of the support structure and rotor wakes. However, the method introduced a large force and relatively high TKE when compared with the experimental data, which in turn increased the far wake mean velocity deficit. This behaviour is attributed to the coarse mesh employed in this work in combination with the lack of boundary-layer modelling in the cell-blocking implementation. Momentum extraction would likely improve with mesh quality.

The widely used AD/AL representation of the nacelle and tower was tested using standard non-dimensional force coefficients from the literature. While the AD nacelle generated a good approximation of the flow when compared with the body-fitted nacelle, the same cannot be said for the AL tower. Representing the tower using an AL was found to not be able to produce a turbulent separated wake given the current parameter set-up. Modifications in the smearing parameter and mesh quality could improve the effectiveness of the method in predicting separated flows.

While maintaining a low-background turbulence intensity characteristic of wind tunnels is well suited to investigating the detailed interactions between the support structure and the rotor wake, higher background turbulence is more realistic for practical applications. With turbulence intensities up to 10%, the influence of the tower reduces in the mid to far wake; however, the influence of the support structure remains significant, even when background turbulence is high especially in the inner parts of the near wake. This effect could have implications on higher order far wake statistics or when using far wake models that utilise the near wake length.

The current study is a significant first step towards understanding and improving the modelling of the interaction between a wind turbine wake and a support structure wake. The NTNU rotor has a large tower-to-rotor diameter ratio and low-background turbulence intensity, conditions ideal for the study the rotor/support structure interaction. Methods from this study may be applied to the study of the interaction between utility-scale rotors and their support structures. It is noted that the tower-to-rotor diameter ratio for utility-scale rotors is half that of the NTNU rotor. Finally, the current study suggests there is opportunity in tuning each of the tested methods for a more accurate prediction of bluff body flows.

Acknowledgements

The authors would like to acknowledge the use of the University of Oxford Advanced Research Computing (ARC) facility in carrying out this work https://doi.org/10.5281/zenodo.22558. We also acknowledge Dr David D. Apsley for his discussions and insights into the cell-blocking method. M.Z. would like to acknowledge the support of RWE Renewables and the Department of Engineering Science of the University of Oxford. C.R.V. acknowledges the support of the UKRI through his Future Leaders Fellowship MR/V02504X/1. R.H.J.W. would like to acknowledge EPSRC who supported his fellowship through Grant Number EP/R007322/1.

Funding

M.Z. would like to acknowledge the support of RWE Renewables and the Department of Engineering Science of the University of Oxford. C.R.V. acknowledges the support of the UKRI through his Future Leaders Fellowship MR/V02504X/1. R.H.J.W. would like to acknowledge EPSRC who supported his fellowship through Grant Number EP/R007322/1.

Data Availability Statement

The data that support the findings of this study are available from the corresponding author upon reasonable request.

Peer Review

The peer review history for this article is available at https://publons.com/publon/10.1002/we.70077.

References

1. P. Veers, K. Dykes, S. Basu, et al., "Grand Challenges: Wind Energy Research Needs for a Global Energy Transition," *Wind Energy Science* 7, no. 6 (2022): 2491–2496, https://doi.org/10.5194/wes-7-2491-2022.

2. Y. Shkara, M. Cardaun, R. Schelenz, and G. Jacobs, "Aeroelastic Response of a Multi-Megawatt Upwind Horizontal Axis Wind Turbine (HAWT) Based on Fluid–Structure Interaction Simulation," *Wind Energy Science* 5, no. 1 (2020): 141–154, https://doi.org/10.5194/wes-5-141-2020.

3. F. Zahle, H. Aagaard Madsen, and N. N. Sørensen, "Evaluation of Tower Shadow Effects on Various Wind Turbine Concepts," in *Research in Aeroelasticity EFP-2007-IIForskningscenter Risoe, Risoe-R No. 1698(EN)*, ed. T. Buhl (Danmarks Tekniske Universitet, Risø Nationallaboratoriet for Bæredygtig Energi, 2009), 11–29.

4. T. Burton, N. Jenkins, D. Sharpe, and E. Bossanyi, *Wind Energy Handbook*, 2nd ed. (John Wiley & Sons Ltd., 2011).

5. F. Pierella and L. Sætran, "Wind Tunnel Investigation on the Effect of the Turbine Tower on Wind Turbines Wake Symmetry," *Wind Energy* 20, no. 10 (2017): 1753–1769, https://doi.org/10.1002/we.2120.

6. M. Debnath, C. Santoni, S. Leonardi, and G. V. Iungo, "Towards Reduced Order Modelling for Predicting the Dynamics of Coherent Vorticity Structures Within Wind Turbine Wakes," *Philosophical Transactions of the Royal Society a: Mathematical, Physical and Engineering Sciences* 375, no. 2091 (2017): 20160108, https://doi.org/10.1098/rsta.2016.0108.

7. M. Sherry, J. Sheridan, and D. Jacono, "Horizontal Axis Wind Turbine Tip and Root Vortex Measurements," in *15th International Symposium on Applications of Laser Techniques to Fluid Mechanics* (Springer, 2010).

8. D. Foti, X. Yang, M. Guala, and F. Sotiropoulos, "Wake Meandering Statistics of a Model Wind Turbine: Insights Gained by Large Eddy Simulations," *Physical Review of Fluids* 1 (2016): 044407, https://doi.org/10.1103/PhysRevFluids.1.044407.

9. S. Kang, X. Yang, and F. Sotiropoulos, "On the Onset of Wake Meandering for an Axial Flow Turbine in a Turbulent Open Channel Flow," *Journal of Fluid Mechanics* 744 (2014): 376–403, https://doi.org/10.1017/jfm.2014.82.

10. A. Abraham, T. Dasari, and J. Hong, "Effect of Turbine Nacelle and Tower on the Near Wake of a Utility-Scale Wind Turbine," *Journal of Wind Engineering and Industrial Aerodynamics* 193 (2019): 103981, https://doi.org/10.1016/j.jweia.2019.103981.

11. X. Yang and F. Sotiropoulos, "A Review on the Meandering of Wind Turbine Wakes," *Energies* 12, no. 24 (2019): 4725, https://doi.org/10.3390/en12244725.

12. C. Santoni, K. Carrasquillo, I. Arenas-Navarro, and S. Leonardi, "Effect of Tower and Nacelle on the Flow Past a Wind Turbine," *Wind Energy* 20, no. 12 (2017): 1927–1939, https://doi.org/10.1002/we.2130.

13. L. Ma, T. Nishino, and A. F. Antoniadis, "Prediction of the Impact of Support Structures on the Aerodynamic Performance of Large Wind Farms," *Journal of Renewable and Sustainable Energy* 11, no. 6 (2019): 063306, https://doi.org/10.1063/1.5120602.

14. R. J. Stevens, L. A. Martnez-Tossas, and C. Meneveau, "Comparison of Wind Farm Large Eddy Simulations Using Actuator Disk and Actuator Line Models With Wind Tunnel Experiments," *Renewable Energy* 116, no. Part A (2018): 470–478, https://doi.org/10.1016/j.renene.2017.08.072.

15. D. Foti, X. Yang, L. Shen, and F. Sotiropoulos, "Effect of Wind Turbine Nacelle on Turbine Wake Dynamics in Large Wind Farms," *Journal of Fluid Mechanics* 869 (2019): 1–26, https://doi.org/10.1017/jfm.2019.206.

16. D. Apsley, T. Stallard, and P. Stansby, "Actuator-Line CFD Modelling of Tidal-Stream Turbines in Arrays," *Journal of Ocean Engineering and Marine Energy* 4 (2018): 259271, https://doi.org/10.1007/s40722-018-0120-3.

17. P. Krogstad and P. E. Eriksen, "'Blind Test' Calculations of the Performance and Wake Development for a Model Wind Turbine," *Renewable Energy* 50 (2013): 325–333, https://doi.org/10.1016/j.renene.2012.06.044.

18. "OpenFOAM ESI," (2006), https://www.openfoam.com/.

19. H. Sarlak, C. Meneveau, and J. Sørensen, "Role of Subgrid-Scale Modeling in Large Eddy Simulation of Wind Turbine Wake Interactions," *Renewable Energy* 77 (2015): 386–399, https://doi.org/10.1016/j.renene.2014.12.036.

20. R. Poletto, T. Craft, and A. Revell, "A New Divergence Free Synthetic Eddy Method for the Reproduction of Inlet Flow Conditions for LES," *Flow, Turbulence and Combustion* 91 (2013): 1–21, https://doi.org/10.1007/s10494-013-9488-2.

21. NREL, "SOWFA: Simulator fOr Wind Farm Applications," (2012), https://www.nrel.gov/wind/nwtc/sowfa.html.

22. A. Wimshurst, *Tip Flow Corrections for Horizontal Axis Wind and Tidal Turbine Rotors*" (PhD thesis (University of Oxford, 2018).

23. J. N. Sørensen and W. Z. Shen, "Numerical Modeling of Wind Turbine Wakes," *Journal of Fluids Engineering* 124, no. 2 (2002): 393–399, https://doi.org/10.1115/1.1471361.

24. E. Jost, L. Klein, H. Leipprand, T. Lutz, and E. Krmer, "Extracting the Angle of Attack on Rotor Blades From CFD Simulations," *Wind Energy* 21, no. 10 (2018): 807–822, https://doi.org/10.1002/we.2196.

25. M. Zormpa, F. Zilic de Arcos, X. Chen, C. R. Vogel, and R. H. J. Willden, "The Effect of Flow Sampling on the Robustness of the Actuator Line Method," *Wind Energy* 28, no. 1 (2025): e2965, https://doi.org/10.1002/we.2965.

26. H. Sarlak, *Large Eddy Simulation of Turbulent Flows in Wind Energy*" (PhD thesis (DTU Wind Energy, 2014).

27. A. Wimshurst and R. H. J. Willden, "Analysis of a Tip Correction Factor for Horizontal Axis Turbines," *Wind Energy* 20, no. 9 (2017): 1515–1528, https://doi.org/10.1002/we.2106.

28. L. A. Martnez-Tossas, M. J. Churchfield, and S. Leonardi, "Large Eddy Simulations of the Flow Past Wind Turbines: Actuator Line and Disk Modeling," *Wind Energy* 18, no. 6 (2015): 1047–1060, https://doi.org/10.1002/we.1747.

29. N. Troldborg, *Actuator Line Modeling of Wind Turbine Wakes*" PhD thesis (Technical University of Denmark, 2009).

30. P. Jha, M. Churchfield, P. Moriarty, and S. Schmitz, "Guidelines for Volume Force Distributions Within Actuator Line Modeling of Wind Turbines on Large-Eddy Simulation-Type Grids," *Journal of Solar Energy Engineering* 136, no. 3 (2014): 031003, https://doi.org/10.1115/1.4026252.

31. M. Zormpa, A. A. Adam, R. H. J. Willden, and C. R. Vogel, "Actuator Methods for Wind Turbine Wake Predictions on Coarse Meshes," *Journal of Physics: Conference Series* 3016 (2025): 012031, https://doi.org/10.1088/1742-6596/3016/1/012031.

32. L. Davidson, "Large Eddy Simulations: How to Evaluate Resolution," *International Journal of Heat and Fluid Flow* 30, no. 5 (2009): 1016–1025, https://doi.org/10.1016/j.ijheatfluidflow.2009.06.006.

33. S. B. Pope, *Turbulent Flows* (Cambridge University Press, 2000).

34. H. Sarlak, T. Nishino, L. Martnez-Tossas, C. Meneveau, and J. Sørensen, "Assessment of Blockage Effects on the Wake Characteristics and Power of Wind Turbines," *Renewable Energy* 93 (2016): 340–352, https://doi.org/10.1016/j.renene.2016.01.101.

35. S. Muchala and R. H. Willden, "Influence of Support Structures on Tidal Turbine Power Output," *Journal of Fluids and Structures* 83 (2018): 27–39, https://doi.org/10.1016/j.jfluidstructs.2018.08.008.

36. M. de Oliveira, R. Puraca, and B. Carmo, "Blade-Resolved Numerical Simulations of the NREL Offshore 5 MW Baseline Wind Turbine in Full Scale: A Study of Proper Solver Configuration and Discretization Strategies," *Energy* 254 (2022): 124368, https://doi.org/10.1016/j.energy.2022.124368.

37. L. Ma, P. L. Delafin, P. Tsoutsanis, A. Antoniadis, and T. Nishino, "Blade-Resolved CFD Simulations of a Periodic Array of NREL 5 MW Rotors With and Without Towers," *Wind* 2, no. 1 (2022): 51–67, https://doi.org/10.3390/wind2010004.

38. G. De Cillis, S. Cherubini, O. Semeraro, S. Leonardi, and P. De Palma, "POD-Based Analysis of a Wind Turbine Wake Under the Influence of Tower and Nacelle," *Wind Energy* 24, no. 6 (2021): 609–633, https://doi.org/10.1002/we.2592.

39. P. Orlandi and S. Leonardi, "DNS of Turbulent Channel Flows With Two- and Three-Dimensional Roughness," *Journal of Turbulence* 7 (2006): 1–22, https://doi.org/10.1080/14685240600827526.

40. X. Yang and F. Sotiropoulos, "A new Class of Actuator Surface Models for Wind Turbines," *Wind Energy* 21, no. 5 (2018): 285–302, https://doi.org/10.1002/we.2162.

41. Y. T. Wu and F. Port-Agel, "Large-Eddy Simulation of Wind-Turbine Wakes: Evaluation of Turbine Parametrisations," *Boundary-Layer Meteorology* 138 (2011): 345366, https://doi.org/10.1007/s10546-010-9569-x.

42. G. Deskos, *Numerical Simulations of Wind Turbine Wakes*" (PhD thesis (Imperial College London, 2019).

43. E. Kleusberg, R. F. Mikkelsen, P. Schlatter, S. Ivanell, and D. S. Henningson, "High-Order Numerical Simulations of Wind Turbine

Wakes," *Journal of Physics: Conference Series* 854, no. 1 (2017): 012025, https://doi.org/10.1088/1742-6596/854/1/012025.

44. M. Churchfield, S. Lee, S. Schmitz, and Z. Wang, "Modeling Wind Turbine Tower and Nacelle Effects Within an Actuator Line Model," in *33rd Wind Energy Symposium* (AIAA, 2017).

45. P. Krogstad and P. E. Eriksen, *"Blind Test" Workshop Calculations for a Model Wind Turbine*." Tech. Rep. (Department of Energy and Process Engineering, NTNU, 2011).

46. ESI, "Mesh Generation With the snappyHexMesh Utility," (2024), https://www.openfoam.com/documentation/user-guide/4-mesh-generation-and-conversion/4.4-mesh-generation-with-the-snappyhexmesh-utility.

47. T. Mukha, S. Rezaeiravesh, and M. Liefvendahl, "A Library for Wall-Modelled Large-Eddy Simulation Based on OpenFOAM Technology," *Computer Physics Communications* 239 (2019): 204–224, https://doi.org/10.1016/j.cpc.2019.01.016.

48. C. M. Boileau, F. Duchaine, J. C. Jouhaud, and Y. Sommerer, "Large-Eddy Simulation of Heat Transfer Around a Square Cylinder Using Unstructured Grids," *AIAA Journal* 51, no. 2 (2013): 372–385, https://doi.org/10.2514/1.J051800.

49. R. Willden, X. Chen, S. Tucker Harvey, et al., "Tidal Turbine Benchmarking Project: Stage I—Steady Flow Blind Predictions," *Proceedings of the European Wave and Tidal Energy Conference* 15 (2023): 1–10, https://doi.org/10.36688/ewtec-2023-574.

50. D. D. Apsley, "CFD Simulation of Tidal-Stream Turbines in a Compact Array," *Renewable Energy* 224 (2024): 120133, https://doi.org/10.1016/j.renene.2024.120133.

51. V. P. Laan, N. N. Sørensen, P. E. Rthor, J. Mann, M. C. Kelly, and N. Troldborg, "The k- ϵ- f_P Model Applied to Double Wind Turbine Wakes Using Different Actuator Disk Force Methods," *Wind Energy* 18, no. 12 (2015): 2223–2240, https://doi.org/10.1002/we.1816.

52. ESI-OpenCFD, "Actuation Disk," (2021), https://www.openfoam.com/documentation/guides/latest/doc/guide-fvoptions-sources-actuation-disk.html.

53. G. Schewe, "On the Force Fluctuations Acting on a Circular Cylinder in Crossflow From Subcritical up to Transcritical Reynolds Numbers," *Journal of Fluid Mechanics* 133 (1983): 265–285, https://doi.org/10.1017/S0022112083001913.

54. L. A. Martínez-Tossas, M. J. Churchfield, and C. Meneveau, "Optimal Smoothing Length Scale for Actuator Line Models of Wind Turbine Blades Based on Gaussian Body Force Distribution," *Wind Energy* 20, no. 6 (2017): 1083–1096, https://doi.org/10.1002/we.2081.

55. B. Rocchio, U. Ciri, M. V. Salvetti, and S. Leonardi, "Appraisal and Calibration of the Actuator Line Model for the Prediction of Turbulent Separated Wakes," *Wind Energy* 23, no. 5 (2020): 1231–1248, https://doi.org/10.1002/we.2483.

56. Z. Gao, Y. Li, T. Wang, et al., Modelling the Nacelle Wake of a Horizontal-Axis Wind Turbine Under Different Yaw Conditions, *Renewable Energy* 172 (2021): 263–275, https://doi.org/10.1016/j.renene.2021.02.140.